electronic reprint

Journal of
Applied Crystallography
ISSN 0021-8898
Editor: **Gernot Kostorz**

Structure development in aerogel-processed nanocrystalline alkaline earth oxides as revealed by SANS

Vincent A. Hackley, Peter K. Stoimenov, Derek L. Ho, Li Piin Sung and Kenneth J. Klabunde

Journal of
Applied Crystallography
ISSN 0021-8898

Received 28 September 2004
Accepted 12 May 2005

Structure development in aerogel-processed nanocrystalline alkaline earth oxides as revealed by SANS

Vincent A. Hackley,[a]* Peter K. Stoimenov,[b]‡ Derek L. Ho,[c] Li Piin Sung[d] and Kenneth J. Klabunde[b]

[a]Materials Science and Engineering Laboratory, National Institute of Standards and Technology, Gaithersburg, MD 20899-8520, USA, [b]Department of Chemistry, Kansas State University, Manhattan, KS 66506, USA, [c]Center for Neutron Research, National Institute of Standards and Technology, Gaithersburg, MD 20899-8562, USA, and [d]Building and Fire Research Laboratory, National Institute of Standards and Technology, Gaithersburg, MD 20899-8615, USA. Correspondence e-mail: vince.hackley@nist.gov

Nanocrystalline MgO, CaO and SrO were prepared according to a modified aerogel process (AP). Small-angle neutron scattering (SANS) was used to probe the nanoscale structural features of these materials after each stage of the synthetic process, including hydrolysis, supercritical drying and calcining. SANS data were interpreted using a classical analysis involving power-law and Guinier regimes, and by application of the maximum entropy method. Results are compared with previously published structural data based on X-ray diffraction, electron microscopy and gas adsorption. It is found that the gel hydrolysis product suspended in methanol and toluene exhibits rod-like scattering at small length scales. This is consistent with a filiform morphology previously reported for air-dried $Mg(OH)_2$ alcogel, yet SANS data for air-dried alcogels tested in this study indicate no evidence for low-dimensional structure on any length scale. A previous assertion of mass fractal structure in the AP aerogels and oxides was not confirmed by the present data. Instead, surface fractal scattering was found to be the most dominant characteristic feature associated with the SANS data for all AP powders examined. Additionally, MgO and CaO exhibited a correlation peak that corresponds to liquid-like ordering at Bragg length scales of 5.9 nm and 20.3 nm, respectively. These values are roughly consistent with previous independent estimates of primary particle size, suggesting that local packing of primary crystallites is facilitated by the calcination/dehydration process. An alternative interpretation treats these features as Guinier scattering regions. Fitting of results using the unified Guinier/power-law equation yields sphere-equivalent radii for the primary particles that are nearly identical to the Bragg lengths calculated from the positions of the maxima. Air-dried alcogels produced very weak maxima that could be interpreted either as correlation peaks or as Guinier regions. No maxima were observed for aerogel samples. Maximum entropy analysis using a spherical shape factor produced interesting but complex results for the calculated volume size distributions of these materials. Overall, the observed trend shows an increase in structural feature size with increasing metal cation size.

1. Introduction

Alkaline earth oxide nanoparticles exhibit unique and highly reactive surface chemistry. These materials have been studied extensively as destructive adsorbents, catalysts and bioactive agents (Li *et al.*, 1992; Koper & Klabunde, 1993; Klabunde *et al.*, 1996; Stark *et al.*, 1996; Lucas & Klabunde, 1999; Khaleel *et al.*, 1999; Wagner *et al.*, 1999; Stoimenov *et al.*, 2002, 2003; Medine *et al.*, 2002, 2004). It was demonstrated that nanocrystalline materials derive their unique properties not simply from a proportional increase in surface area, but from enhancements in reactivity that are an intrinsic aspect of their nanoscale dimensions (Itoh *et al.*, 1993; Klabunde *et al.*, 1996; Koper *et al.*, 1997; Zhang *et al.*, 1999). The presence of highly energetic unsaturated coordination sites on the surface of nanosize crystallites, for example at edges, corners, point

‡ Present address: Department of Chemistry, University of California Santa Barbara, Santa Barbara, CA 93106, USA.

defects and vacancies, is considered responsible for the observed differences in chemical behavior relative to their macroscopic analogs (Nieves & Klabunde, 1988; Klabunde & Mulukutla, 2001).

Penn & Banfield (1998) have suggested that complex polytype metal oxide structures can form as a result of crystal growth by an oriented aggregation mechanism. This phenomenon may explain the polyhedral morphology observed for aerogel-processed (AP) nanocrystalline MgO (Klabunde *et al.*, 1996), compared with the cubes and hexagonal platelets typical of conventionally produced MgO crystals. The high-resolution electron microscopy (HREM) results of Richards *et al.* (2000) and subsequently Mel'gunov *et al.* (2003) seem to support this growth mechanism for MgO, wherein individual cube-like nanocrystals are seen to associate in preferred crystallographic directions to form larger-scale polyhedral structures exhibiting many corner and edge sites. Thus, texture plays a central role with respect to surface reactivity in nanoscale materials. In addition, the nanoscale morphology determines or influences other properties, such as pore volume, pore size, mechanical strength and dispersion behavior.

Nanocrystalline alkaline earth oxides are readily prepared using the metal alkoxide sol–gel route (see for example Utamapanya *et al.*, 1991; Rywak *et al.*, 1995; Znaidi *et al.*, 1996; Chadwick *et al.*, 1998). The resulting alcogel (metal hydroxide gel suspended in alcohol medium) must be dried and calcined to produce the corresponding oxide. This process can induce structural collapse and crystal growth with loss of porosity and nanoscale features. A modified supercritical drying procedure (Utamapanya *et al.*, 1991) coupled with calcination of the resulting aerogel under dynamic vacuum (see for example Koper *et al.*, 1997), yields a high-surface-area high-porosity metal oxide with powder-like macroscopic consistency and containing primary crystallites in the nanosize regime: typically 4 to 20 nm. The nanoscale structural evolution associated with this synthetic route can be dependent on a number of different factors during various stages of the process. For instance, the metal alkoxide/solvent ratio used during hydrolysis, the solvent composition, and the temperature and rate of temperature increase during autoclaving and calcining all have important influences on structure development, from the atomic scale to the microscale. These factors determine not only the primary crystallite size and shape, but also the manner in which primary crystallites coalesce into larger structures. These physical characteristics can impact the chemical reactivity, reaction efficiency, adsorptive capacity, transport properties, and formulation of these materials for industrial, environmental or biotechnology applications.

The modified AP route has been employed to produce pure oxides of several Group II cations, namely Mg, Ca and Sr. BaO cannot be prepared using the modified AP procedure as $Ba(OH)_2$ melts before its decomposition to the oxide form. A number of previous studies have reported structural data for these materials, based primarily on X-ray diffraction (XRD), transmission electron microscopy (TEM) and gas adsorption measurements. These results serve as a starting point for understanding the structural evolution in these systems, and provide context for interpretation of the present scattering experiments. A brief review of this body of work is therefore useful, beginning with the well studied AP MgO system.

Diao *et al.* (2002) reported XRD data for an alcogel derived from $Mg(OCH_3)_2$ and then air-dried, showing highly broadened and distorted peaks that indicate the presence of $Mg(OH)_2$ (brucite) and the partial hydrolysis product $Mg(OH)(OCH_3)$. Mel'gunov *et al.* (2003) also found substantial methoxide presence in AP-derived $Mg(OH)_2$ ($\sim$20% mass fraction methanol), but determined that it was entirely surface-bound with a site density similar to that predicted for Mg^{2+} ions at the crystal surface ($\sim$5.2 groups per nm^2). Combined TGA/GCMS analysis shows that methanol is slowly expelled over a temperature range from about 453 to 703 K. It has been suggested (Koper *et al.*, 1997) that the presence of residual methoxide groups may help stabilize nanocrystallites against coalescence and sintering during subsequent dehydration and calcining, and their presence appears to be ubiquitous in sol–gel-prepared MgO precursors (Rywak *et al.*, 1995). TEM analysis showed that the air-dried alcogel consists of a fine mesh structure lacking any obvious crystalline habit. Utamapanya *et al.* (1991) reported XRD results for the supercritically dried $Mg(OH)_2$ that indicate it contains a poorly crystallized mixture of brucite and periclase, but these results do not rule out the presence of a transitional pseudomorphic phase containing a partially dehydrated material. Hexagonal brucite often forms fibrous aggregates and foliated masses, and is known to pseudomorph periclase (Wyckoff, 1963) with a stoichiometric mass loss of 30.8% and a 54.3% reduction in the molar volume. In the data of Utamapanya *et al.* (1991), the characteristic periclase XRD peaks are shifted down compared with the AP oxide. Their XRD data for the calcined aerogel shows broadened but less distorted peaks that clearly identify the material as periclase. Analysis of XRD line broadening using the Scherrer equation gives a crystallite size of about 3 to 4 nm for the aerogel (Utamapanya *et al.*, 1991) and 4 to 5 nm for the calcined MgO powder (Utamapanya *et al.*, 1991; Richards *et al.*, 2000). TEM images of AP MgO (Itoh *et al.*, 1993; Koper *et al.*, 1997) suggest that the calcined product retains some topological similarity with the filiform morphology observed in the air-dried alcogel. Under higher magnification, individual crystallites appear as irregular polyhedrals with a fairly uniform size (Itoh *et al.*, 1993; Klabunde *et al.*, 1996), while the surface of these crystals appears rough. Using HREM, Richards *et al.* (2000) showed that these polyhedrals are formed by the coalescence of 1 to 3 nm planar-cubic crystallites. The cubic nanocrystals are shifted along the [001] coalescence face, which gives rise to step-like features on the surface; hence the rough appearance at lower magnifications. Also apparent are chain-like interconnected quasi-linear arrays of cubic platelets that have partially coalesced. These latter structures may form the backbone that provides strength and cohesion to the micrometer-scale porous 'aggregates' visible under low magnification. Mel'gunov *et al.* (2003) also report HREM results

Table 1
Physical property data reported for aerogel (hydroxide) and calcined aerogel (oxide) powders.

Specific surface area, pore diameter and porosity determined by N_2 gas adsorption method are presented. To estimate porosity from adsorption data, the following skeletal densities (g cm^{-3}) were used: $Mg(OH)_2$ aerogel (2.36), MgO (3.58), CaO (3.34) and SrO (5.10). Crystallite size was determined from analysis of XRD line broadening using the Scherrer equation.

	Mg[a–f]		Ca[b–d,g]		Sr[c,h]	
	Aerogel	Calcined	Aerogel	Calcined	Aerogel	Calcined
Surface area (m^2 g^{-1})	800–1000	300–500	30–140	70–160	–	16–19
Pore diameter (nm)	10	5–21	–	4–100	–	13
Estimated porosity (%)	68	71–87	–	40–67	–	20–24
Crystallite size (nm)	3–4	4–5	13	7–8	–	21

References: (*a*) Utamapanya *et al.* (1991); (*b*) Klabunde *et al.* (1996); (*c*) Medine *et al.* (2004); (*d*) Richards *et al.* (2000); (*e*) Itoh *et al.* (1993); (*f*) Mel'gunov *et al.* (2003); (*g*) Koper *et al.* (1997); (*h*) Medine *et al.* (2002).

showing step-like overlapping assemblies of primary MgO cubic crystallites, with aggregation proceeding preferentially in the [100] and [110] directions. Nitrogen gas adsorption measurements on AP MgO reported by Itoh *et al.* (1993) yield a relatively uniform pore volume distribution with a peak near 5 nm and an upper cut-off of 10 nm. These pores are attributed to the void space formed between consolidated polyhedra.

A smaller body of work exists for AP CaO and AP SrO. XRD and TEM results indicate that AP CaO follows a similar structural evolution to that of MgO, but the key structural characteristics exist on a larger scale when Ca is the cation (see Table 1). For instance, Koper *et al.* (1997) found that for AP $Ca(OH)_2$ and AP CaO, crystallite size is generally larger by a factor of 2 to 4 compared with their Mg counterparts, while gas adsorption measurements yield a pore volume distribution with broad overlapping peaks between 3 nm and 100 nm for AP CaO. More recently, using an identical synthetic route, Medine *et al.* (2004) reported an average pore diameter of 13 nm for AP CaO. A review of the literature suggests that small variations in the synthesis conditions can have a significant impact on the final surface area and porosity of these materials. This is particularly true for CaO, where a 'blossoming' effect has been noted during thermal dehydration under vacuum (Koper *et al.*, 1997). This temperature-dependent phenomenon is accompanied by an increase in surface area and a decrease in crystallite size upon dehydration: a counterintuitive result. This behavior has been attributed to the formation of channels between isolated crystallites and to rapid removal of water vapor to minimize steam induced sintering. Itoh *et al.* (1993) reported a similar effect for MgO, but in this case the increase in surface area was less pronounced and was reversed by the onset of sintering above 573 K. In striking contrast to the other oxides, AP SrO develops an unusual texture. Medine *et al.* (2002) described AP SrO as nanocrystalline in the form of 'brush-like collections of metal oxide fibers'. Apart from the fibrous component, which may be a general characteristic associated with AP alkaline earth oxides, HREM shows unusual nanoscale morphology for SrO, which Medine *et al.* have termed 'fish-like'. The primary crystallites consist of roughly 100 nm elongated particles, which are composed of a dense center, consisting of closely packed, 2 to 6 nm, oriented cubic blocks, and two extensions consisting of multiple stalactitic protuberances that have undergone homoepitaxial growth on the central body. The needles and central body are oriented along the [100] direction, producing what might more correctly be termed as crab-like morphology. Gas adsorption gives a pore volume distribution diameter of about 13 nm, while XRD yields a crystallite size of about 21 nm. The primary crab-like particles are randomly associated in larger-scale porous assemblies of undefined size.

Thus, the general trend is an increase in the characteristic structural dimensions with increasing cation size, in going from Mg to Ca to Sr. Although this trend may establish itself early in the aerogel process, possibly during the initial hydrolysis reaction, subsequent processing steps obviously play a critical role in determining the final nanoscale and microscale architecture of the AP oxides. These materials display evidence of hierarchical structure with multiple structural levels that may be physically coupled or independent.

We are aware of two previous studies on AP alkaline earth oxides in which small-angle scattering data were reported. Richards *et al.* (2000) performed small-angle X-ray scattering (SAXS) measurements on AP MgO and AP CaO powders and compressed pellets, while Diao *et al.* (2002) used SAXS to study structure in precursor alcogels as a function of the toluene/methanol ratio. Neither of these studies relied heavily on scattering data, and as a result the published work was limited in both quantity and scope. Their results will be discussed in relation to the present work.

In this study, we employ small-angle neutron scattering (SANS) to probe structural features in the nanoscale regime. In order to chart the evolution of structure in this system, we carried out SANS measurements at each stage of the synthetic process for three Group II cations: Mg, Ca and Sr. Identical processing conditions were used in each case, and the samples examined include liquid-phase and air-dried alcogels, supercritically dried alcogels and calcined aerogel powders. SANS data are interpreted using both simple scaling arguments and application of particle-based scattering models, including the maximum entropy method (Potton *et al.*, 1988). Results are compared with previously published structural data based on XRD, TEM and gas adsorption. Additionally, the present data are examined within the context of noncrystalline silica aerogels, which are extensively reported in the literature. The

apparent effect of cation size on structure development in this system is addressed implicitly.

2. Experimental section

2.1. Materials

Metal oxide nanoparticles of Mg, Ca and Sr were prepared using a sol–gel/supercritical drying process. The synthetic route has been described previously for MgO (Utamapanya *et al.*, 1991), CaO (Koper & Klabunde, 1993; Koper *et al.*, 1997) and SrO (Medine *et al.*, 2002). The approach involves four sequential steps: (i) preparation of a metal alkoxide solution, (ii) hydrolysis, (iii) supercritical drying, and (iv) calcination under dynamic vacuum. The metal alkoxide solution is prepared by dissolving the corresponding metal in methanol in the presence of toluene as a spectator solvent. Hydrolysis is performed under inert gas atmosphere by the gradual addition of an excess of high-purity deionized water, resulting in an opaque gel suspension containing $M(OH)_2$ polycondensation product (where M = Mg, Ca or Sr). The gels are then dried in an autoclave (Parr, 4560 Series[1]), during which the system is flushed with nitrogen and heated to 538 K to yield a final pressure of approximately 6900 kPa. The sample is continually mixed in the autoclave during the drying process. The autoclave is then vented to evacuate the solvent. Supercritical drying produces a fine powdery material, characterized by a high specific surface area (see Table 1). Calcination is performed at 773 K under dynamic vacuum in a Schlenk tube for 8 h to produce the final oxide aerogel product.

Additionally, the hydroxide gel suspensions were allowed to air-dry slowly in small glass vials at ambient temperature for 8 days. In the case of Mg and Ca, this resulted in the formation of solid-like gels, which became liquefied upon vigorous shaking. For Sr, the alcogel separated into two phases, with clear solvent over a concentrated gel layer; the solvent layer was decanted during the drying process. All three samples were then transferred to Pyrex dishes and allowed to dry for an additional 24 h. This resulted in a dry white flaky material in the case of Mg and Ca, and a dry white fluffy material in the case of Sr. The powders were placed in an oven and dried under vacuum for 24 h at 333 K. Samples were then stored in a desiccator until needed for SANS measurements.

2.2. SANS experiments

SANS measurements were performed using the pinhole-collimated NG-7 30 m SANS instrument (see Glinka *et al.*, 1998, for details of instrument design and operation) at the NIST Center for Neutron Research (NCNR) over a maximum q range from 0.00089 to 0.505 Å^{-1}. The neutron wavelength was 6 Å with a resolution $\Delta\lambda/\lambda = 0.11$, and the sample aperture was 1.27 cm. Each sample was measured in two different instrument configurations, characterized by nominal sample-to-detector distances of 1.0 m and 15 m. The alcogels and aerogel powders were also measured using a neutron focusing lens at 15.3 m (see Choi *et al.*, 2000), which extends the low-q resolution compared with conventional pinhole collimation. Data were collected using a 64 × 64 cm position-sensitive proportional counter and converted to circularly averaged one-dimensional data as intensity, $I(q)$, *versus* momentum transfer, $q = 4\pi/\lambda \sin(\theta/2)$, where θ is the scattering angle. The individual runs were then combined into a single curve, using available data reduction macros based on the *IGOR Pro* data analysis package (Wavemetrics, Oregon USA). The scattered intensity was corrected for detector efficiency, background and parasitic scattering (National Institute of Standards and Technology Center for Neutron Research, 2002). The incoherent scattering from the samples was estimated from the flat background in the high-q range.

Samples for analysis were placed into demountable titanium cells fitted with quartz windows and a 1 mm path length. The sample volume was approximately 0.4 ml. Alcogel suspensions were allowed to settle overnight, then the concentrated gel was extracted from the bottom of the sample vial using a Pasteur pipette. The concentrate was then injected into the SANS cell and sealed prior to the measurement. Cells were mounted on a remote-controlled multi-sample block in the neutron beam.

2.3. Data analysis

Scaling arguments and numerical approximations, in conjunction with scattering models, can be utilized to extract useful microstructural parameters from the experimental SANS data. These parameters can then be used to characterize length-scale-dependent structural changes with respect to the synthesis process.

Aerogel-produced porous materials typically exhibit power-law scattering over limited ranges, where $I(q) \simeq q^{-\alpha}$, and α is the power-law exponent whose value is a function of the characteristic morphology of the material over a length scale defined by q; a rough criterion for small-angle scattering is that a length π/q is associated with scattering at a given value of q (Schmidt, 1988), and we utilize that criterion in the present work. Integer values for α often reflect well defined geometries, such as rods ($\alpha = 1$) or sheets ($\alpha = 2$) (see Porod, 1982), while a non-integer value observed over a wide q range can imply the presence of statistically scale-invariant (fractal) morphology (for an overview of these concepts see Schaefer, 1989). In brief, a mass fractal is an object that scales with length in three-dimensional space with an exponent that is less than 3 (*i.e.* $M \simeq r^D$, where $D < 3$). Mass fractals are said to be self-similar, since their characteristic irregular patterns remain isotropically invariant under changes in scale (though typically over a limited length scale range). Likewise, a surface fractal scales in two-dimensional space but with an exponent that is greater than 2. A fractal surface is said to be self-affine, because the scale invariance is anisotropic; for small-angle

[1] Certain trade names and company products are mentioned in the text or identified in illustrations in order to specify adequately the experimental procedure and equipment used. In no case does such identification imply recommendation or endorsement by National Institute of Standards and Technology, nor does it imply that the products are necessarily the best available for the purpose.

scattering this means there are no three-dimensional re-entry convolutions. The appearance of non-integer power-law scattering is not definitive proof of underlying fractal structure; apparent power-law scattering could result, for instance, from a combination of closely overlapping structural regimes (Beaucage, 1995). Therefore the extent of the power-law regime is an important determinant for fractal character.

Power-law dependence in the final part of the scattering curve provides information about the internal surface of a porous material (Porod, 1982; Bale & Schmidt, 1984). Additionally, the Guinier approximation (see Guinier & Fournet, 1955) can be applied if discrete scattering domains exist (*e.g.* particles or pores). The Guinier formula describes an exponential decay in $I(q)$, where the radius of gyration of the scatterer, R_g, can be obtained from the slope of a plot of $\ln I(q)$ *versus* q^2 (the so-called Guinier plot).

Selected data sets were fit using the unified approach of Beaucage (1995, 1996). The unified equation is an approximate form that describes one or more structural levels, each having an associated Guinier regime (describing a characteristic domain size) and a structurally limited power-law regime (describing the mass- or surface-fractal scaling for that level). Using Beaucage's nomenclature, the unified equation for a single structural level is then

$$I(q) = G\exp\left(\frac{-q^2R_g^2}{3}\right) + B\left\{\left[\operatorname{erf}\left(\frac{kqR_g}{6^{1/2}}\right)\right]^3 \Big/ q\right\}^P, \quad (1)$$

where G and B are Guinier and power-law prefactors, respectively, k is an empirical constant with a value close to 1, and P is the power-law exponent (equivalent to α). With the inclusion of appropriate cut-offs for power-law behavior, equation (1) can be extended to describe any number of interrelated structural levels. To fit the SANS data, we have used a version of this model implemented by Ilavsky (2004) in the *Irena 1.7* macro package for *Igor Pro*. In this model, there are six adjustable parameters for each level: R_g, G, P, B, RGCO and a flat background. RGCO is the high-q cut-off for power-law dependence, and can be linked to the R_g value of the lower (underlying) level; for level 1 (the lowest level) RGCO is set to zero. Interactions between correlated domains are not considered in our analysis. The best fits are obtained by a systematic optimization process that begins by estimating initial parameter values through local fits of possible Guinier and power-law regions in the data.

In addition, we chose the maximum entropy approach (Potton *et al.*, 1988) to analyze the SANS data in terms of scattering from an uncorrelated collection of homogenous spheres. Maximum entropy determines a unique solution for the size distribution without depending on an empirical function, and it produces a solution that is everywhere positive. In this context, entropy (disorder) is statistically related to the broadness and uniformity of the distribution. Thus, the maximum entropy size distribution represents the most uniform and least biased solution consistent with the available data. To fit the SANS data we used the *MaxEnt* algorithm (Jemian, 1995) in the *Irena 1.7* macro package. *MaxEnt* is based on the *MAXE* code from UKAEA Harwell Laboratory. Details regarding the application of *MAXE* and its limitations can be found in the appendix of Long *et al.* (1990). Input parameters are the aspect ratio (1 for a sphere), scattering contrast (important only for obtaining calibrated results), error multiple, and flat background. In addition, the fit is influenced by the input q range, the upper and lower size limits for the distribution, and the number and spacing of size bins. We used 100 logarithmically spaced bins for the calculated size distributions. To obtain the best fit, the aspect ratio, background, fitting range and size distribution limits were varied independently while attempting to minimize the error multiple. The purpose of the error multiple is to correct for poorly estimated errors in the input data, which it does by relaxing the fit requirements. By increasing this parameter, convergence can be forced for a given analysis, providing both a means for fine tuning the other adjustable parameters and a measuring stick for the quality of the input data with respect to the assumptions of the underlying physical model. Convergence occurs when the statistical parameter χ^2 equals the number of data points, N, and configurational entropy is maximized. The normalized residuals are a measure of the goodness of fit. If the data are underfit, the residuals will be non-random, while the $\chi^2 = N$ condition prevents overfitting (Tatchev & Kranold, 2004). The model output is the differential volume distribution (dV/dD) as a function of particle diameter.

3. Results and analysis

3.1. Precursor alcogel

The addition of excess water to the methoxide solution generates large gel particles of hydrated metal hydroxide suspended in methanol and toluene. These gel particles, precursors to the aerogel powders, were analyzed both in the wet state and after air-drying under ambient conditions. Fig. 1

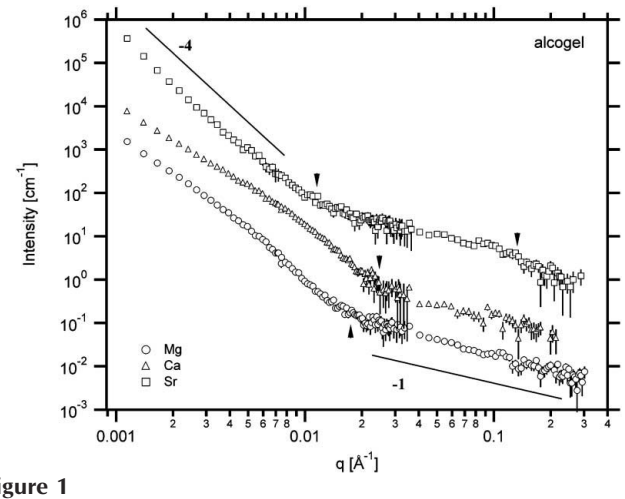

Figure 1
SANS results for metal hydroxide gels suspended in a solution of methanol and toluene. Markers indicate inflections and limits to power-law regimes as discussed in the text. Numerical values are slopes of lines drawn for comparison purposes.

Table 2
Scattering exponents determined from a linear least-squares analysis of high-q power-law regions in the SANS data.

	High-q scattering exponent, α			
	Alcogel	Air-dried alcogel	Aerogel	Calcined aerogel
Mg	1.21 ± 0.02	2.99 ± 0.01	3.61 ± 0.02	∼4
Ca	1.17 ± 0.13	3.43 ± 0.03	3.32 ± 0.11	?
Sr	1.00 ± 0.06	3.53 ± 0.05	3.66 ± 0.07	3.68 ± 0.01

shows log–log plots of the alcogel SANS data for each cation in the series. The curves are visually similar and exhibit limited power-law behavior. Due to rather large incoherent contributions and weak contrast with the protonated solvent phase, the high-q data are unusually noisy for these samples; however, in general, the region appears to scale with a power-law exponent, α, close to unity. Least-squares fits (see Table 2) yield exponents of 1.2, 1.2 and 1.0, for Mg, Ca and Sr, respectively. The Sr curve shows a possible high-q inflection with the slope steepening as one would expect when $\xi_1 q > 1$, where ξ_1 is the lower size cut-off for fractal scaling and should approximate the size of the primary building blocks. For Sr a value of $\pi/q = 2.3$ nm can be assigned to ξ_1, while for Mg and Ca the linear behavior extends beyond the upper q limit, thus approaching molecular dimensions ($\pi/q < 1$ nm).

A well defined inflection is also apparent in the intermediate q range, lying roughly between 0.01 and 0.02 Å^{-1}. This inflection provides an upper size cut-off, ξ_2, for the linear structures of the order of $\pi/q \simeq 12$ to 16 nm for Mg and Ca, and about 30 nm for Sr. Below the primary inflection, scattering curves are much steeper with slopes approaching −4. Exponents between 3 and 4 can be interpreted as scattering from rough surfaces (Bale & Schmidt, 1984) with a corresponding surface dimensionality $D_S = 6 - \alpha$. However, these regions are not well defined, and for Mg and Ca the curves bend toward a lower slope at q values below about 0.006 Å^{-1} ($\pi/q \simeq 52$ nm). This could indicate the presence of a third level

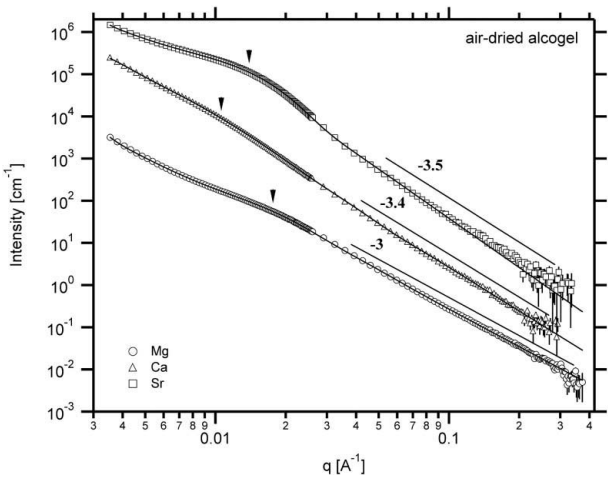

Figure 2
SANS data for air-dried hydroxide gels. Markers indicate locations of inflections or maxima discussed in the text. Numerical values are slopes of lines drawn for comparison purposes.

of structure at dimensions encroaching on the micrometer scale or a very broad range of gel domain sizes may exist leading to an extended Guinier region at low q. One can infer from the lack of a plateau in the inner portion of the scattering profiles that large (micrometer scale) structures do exist, but the instrument resolution is not adequate to probe these larger dimensions fully. The Sr curve shows Porod law behavior at the low-q instrumental limit, suggesting the existence of fairly massive non-mass-fractal domains with a sharp interface.

Ambient evaporation of the gel suspension with subsequent vacuum drying yielded dramatically altered scattering profiles (Fig. 2), with much better defined scaling regimes covering in excess of a decade in q. Accompanying these changes are an improved contrast and a significant reduction in incoherent scattering (due to removal of the protonated solvent and some likely dehydration of the solid phase during vacuum treatment). The power-law exponents characteristic of the low-dimensional nanoscale morphology observed for the liquid gel are completely absent after drying. Instead one observes high-q exponents ranging between 3 and 3.5 (see Table 2), values normally indicative of scattering from fractally rough surfaces and yielding D_S values of 3.0, 2.6 and 2.5 for Mg, Ca and Sr, respectively. Although power-law exponents near 3 are not commonly observed in aerogel systems, Vacher *et al.* (1988) reported values close to 3 for silica aerogels prepared under neutral conditions and interpreted this as scattering from an extremely rough fractal surface. Following treatment of the silica at 773 K, the exponents increased to 4, indicating that the surface roughness was smoothed out and apparently confirming the surface fractal origin for scattering in the untreated samples. In another example, Keefer & Schaefer (1986) observed a continuous increase in α from about 2.8 to 3.6 with increasing water content for silica 'polymers' grown under alkaline conditions. They attributed the increase to a transition from mass fractal to surface fractal characterized by a maximally folded surface.

The power-law regimes in Fig. 2 extend from near molecular length scales up into the 10 to 30 nm range. An inflection or maximum marks the low-q limit of power-law behavior. For Mg and Ca, these inflections could be interpreted as exponential regions obeying Guinier's approximation, though partially obscured by overlapping structural levels. On the other hand, for Sr this feature clearly suggests a correlation peak broadened by irregular arrangement and centered at $q \simeq 0.014$ Å^{-1}, which corresponds to a Bragg diffraction distance, $d = 2\pi/q$, of about 45 nm.

Like their suspended alcogel counterparts, the scattering curves for the air-dried alcogels continue to rise at the lowest experimentally reachable q value, suggesting the presence of large scattering domains (>400 nm).

The overall form of the scattering profiles in Fig. 2 suggests the possibility of coupled structural levels, and therefore we have attempted to fit these data using the unified Guinier/power-law equation. The best fit to the SANS data for the dried gels was obtained using two structural levels with RGCO unlinked. The resulting fits are overlaid (solid line) on the data in Fig. 2. Reasonably good fits were obtained for both Mg and

Table 3
Structural parameters determined by fitting SANS data using the unified Guinier/power-law equation for selected air-dried alcogels and calcined aerogels.

		Structural level 1			Structural level 2		
	Flat background (cm^{-1})	R_g (nm)	P	RGCO (nm)	R_g (nm)	P	RGCO (nm)
Air-dried alcogels							
Mg	0.119	11.0 ± 0.04	2.95 ± 0.02	0	116 ± 8	3.10 ± 0.01	3.7
Ca	0.055	7.0 ± 0.10	3.44 ± 0.02	0	69 ± 1	2.77 ± 0.01	9.9
Sr	0.021	14.0 ± 0.02	3.88 ± 0.01	0	139 ± 30	2.74 ± 0.02	14.0
Calcined aerogels							
Mg	0.002	2.2 ± 0.01	4 (fixed)	0	68 ± 1	3.82 ± 0.01	2.2†
Mg	0.004	2.3 ± 0.01	5.00 ± 0.03	0	64 ± 1	3.91 ± 0.01	2.3†
Ca	0.005	7.3 ± 0.05	4.00 ± 0.05	0	85 ± 7	3.52 ± 0.01	7.3†

† RGCO linked to R_g for level 1.

Ca over most of the experimental q range, with residuals largely under 3%. For Sr the fit appears reasonably good overall, except for some mismatching above $q = 0.13$ Å^{-1}, but the residuals were higher (up to about 5%). All unified equation fits produced non-random residuals over much of the fitted range, but this was especially noticeable near the maxima, which underscores the likelihood that these features are correlation effects rather than Guinier scattering regions. The calculated structural parameters are given in Table 3. The R_g values for structural level 1 seem reasonable, but the values for level 2 are dubious since neither a second Guinier region nor a fully developed power-law region is apparent at low q.

3.2. Supercritically dried aerogel powder

Like the previous subcritical air-dried samples, supercritical drying of the alcogels at 538 K leads to substantially modified scattering profiles dominated by apparent surface fractal scaling at high q (see Fig. 3 and Table 2). Unlike air-dried gels, the form of the scattering curves is distinctly dissimilar for each cation following supercritical removal of the solvent. In particular, the curve for Ca is unusual, and suggests the presence of two overlapping, and perhaps independent, structural regimes.

Except for Mg, which exhibits no clear inflection point, the primary inflection marking the transition between two structural regimes is shifted to higher q (*i.e.* smaller length scales) relative to the air-dried analogues. The Sr aerogel has the coarsest structure of the three samples, with an apparent Porod slope extending into micrometer length scales at low q. The high-q power-law exponents yield D_S values of 2.4, 2.7 and 2.3 for Mg, Ca and Sr, respectively. Surface fractal behavior apparently extends down to molecular dimensions for Mg and Ca; Sr data are truncated at high-q due to the large incoherent background correction. An alternative interpretation of scattering exponents between 3 and 4 for a porous body is based on power-law polydispersity in pore size (Pfeifer & Avnir, 1983; Martin, 1986), but surface fractal scaling and pore polydispersity are geometrically equivalent and difficult to differentiate experimentally.

3.3. Calcined aerogel powder

Fig. 4 shows the SANS data for the three calcined aerogel powders. MgO and CaO exhibit new features that appear to be correlation peaks centered near $q = 0.107$ Å^{-1} and 0.031 Å^{-1}, respectively. These maxima correspond to ordering at d = 5.9 nm and d = 20.3 nm for MgO and CaO, respectively. With the exception of SrO, whose scattering curve appears similar in form to the precursor aerogel curve (but with an extended power-law range), there is no obvious continuity between the data in Fig. 3 and the corresponding curves in Fig. 4.

For MgO, the final slope is obscured by the correlation peak and truncated at high q, but a good fit was obtained using a Porod decay with a power-law exponent of 4. CaO shows two possible power-law regions, one at low q and one at high q, but neither region is fully developed. The low-q exponent approaches 3.6, suggesting surface fractal scaling similar to SrO, but at length scales above about 40 nm. The high-q scatter prevents the assignment of a precise value for the exponent, but α is apparently less than 4. In contrast, SrO exhibits a very broad and well developed power-law region,

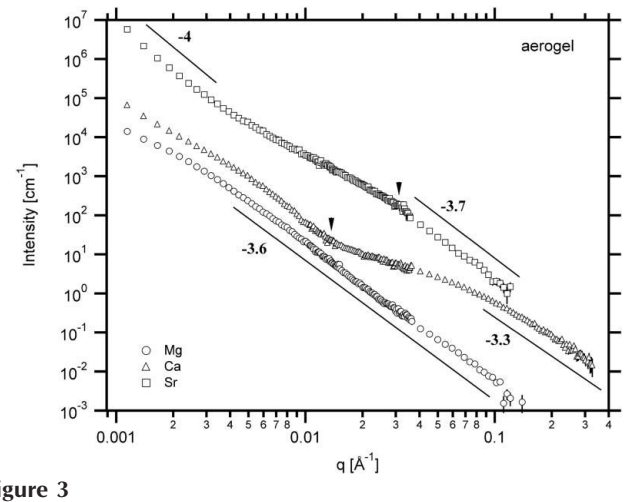

Figure 3
SANS data for supercritically dried metal oxide/hydroxide aerogel powders. Markers indicate locations of inflections or demarcations discussed in the text. Numerical values are slopes of lines drawn for comparison purposes.

spanning more than a decade in q and representing length scales from about 34 nm down to less than 1 nm. At low q the slope rises strongly, indicating that higher order structure exists beyond the resolution of this experiment. We speculate that such a sharp increase in slope (apparent $\alpha > 5$) at low q could be associated with the high-q side of a correlation peak existing below the experimental threshold. If this assumption is correct, then the correlation length would be on the order of several hundred nanometers, an order of magnitude greater than the length scales associated with MgO and CaO. Clearly, by any measure, SrO contains the coarsest structural features of the three AP oxides, following a trend established in the precursor materials.

Because the scattering curves for MgO and CaO show features possibly associated with hierarchical particulate structures (*i.e.* more than one power-law region separated by an inflection), we chose to fit these data using the unified Guinier/power-law equation with two structural levels; the SrO curve did not exhibit sufficient feature complexity to warrant this type of analysis. The calculated structural parameters for these fits are given in Table 3, while the actual fits are overlaid on the SANS data in Fig. 4. Based on prior analysis, MgO data were initially fit with the assumption of a sharp interface ($P = 4$) for the lowest structural level. Following this, a second fit was performed in which P was allowed to vary. In the latter case, a power-law exponent of 5 was obtained. Slopes steeper than Porod's law are characteristic of a broadened or diffuse interface (Schmidt, 1988), though that seems unlikely in the present case. Regardless, the choice of a final slope had little effect on the Guinier portions of the fit, and the calculated value of R_g for either structural level was virtually identical when P was either fixed or allowed to vary. For CaO, where the maximum is shifted toward lower q values relative to MgO, the fit produces a power-law exponent of 4 for level 1, but visually the fit appears poorly mismatched above $q = 0.1$ Å^{-1} and the residuals are highly non-random over this range. The R_g for the primary particle calculated by the unified model fit yields a spherical diameter, $d_s = 2R_g[(5/3)^{1/2}]$, of 5.8 nm and 19 nm for MgO and CaO, respectively.

3.4. Maximum entropy results

Fig. 5 shows, as a representative example, the results obtained from the maximum entropy analysis of SANS data for the $Mg(OH)_2$ alcogel. In contrast to other attempts we made to model the broad range of structural topographies and length scales represented by this group of materials (including the unified equation, particle interference models, and a fractal model), *MaxEnt* fit the data consistently well for all samples, making comparisons between samples much more convenient. This does not imply that maximum entropy is necessarily the most accurate model for this system, but within the constraints of the model parameters we found that *MaxEnt* produces the most consistent results. Residuals for the most part lie within ±2% and appear largely random with a few exceptions. Non-random residuals show up primarily at the extreme limits of the fitted q range (especially at the low-q limit). It is reasonable to assume that some distortion of the calculated distribution occurs due to truncation of the low-q range, as reported by Long *et al.* (1990); however, the nanosize regime is well represented by the experimental q range, so we anticipate little influence on this portion of the calculated distribution. Small non-random residuals were also observed on the high-q side of the maxima associated with some of the air-dried and calcined powders. This is not too surprising, since these features are believed to result from correlation effects, and independent scattering is a basic prerequisite of the maximum entropy model. The degree to which correlation

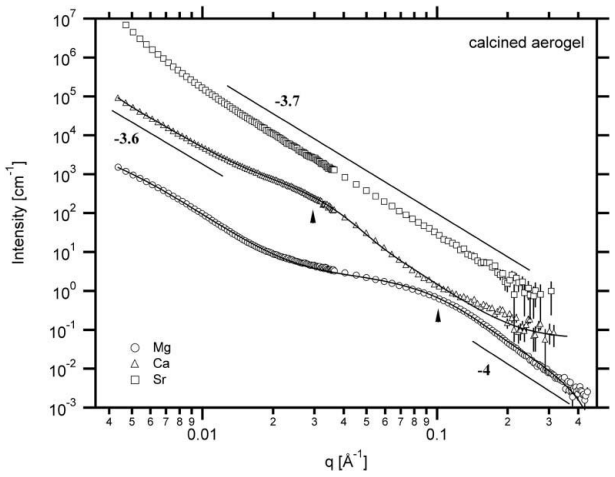

Figure 4
SANS data for calcined metal oxide aerogels. Markers indicate locations of maxima discussed in the text. Numerical values are slopes of lines drawn for comparison purposes.

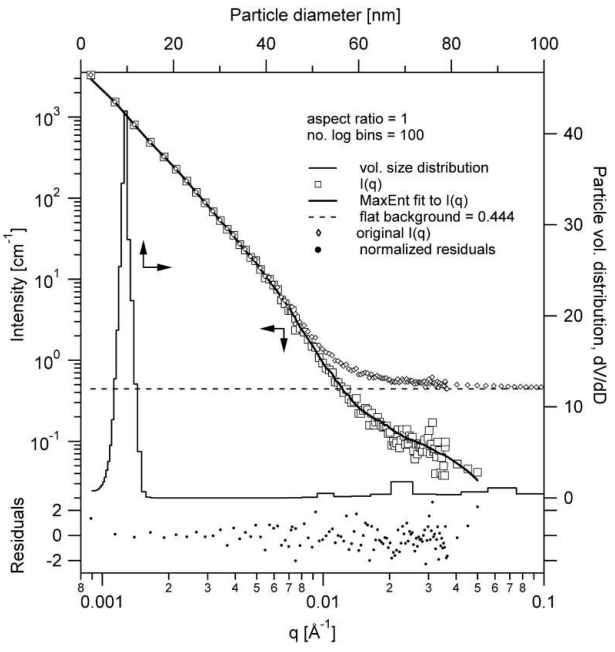

Figure 5
Results from the maximum entropy fit of SANS data for the $Mg(OH)_2$ alcogel, showing the calculated volume size distribution (dV/dD), the *MaxEnt* fit and residuals.

Table 4
Summary of maximum entropy results for fits of SANS data using the *MaxEnt* code with a spherical shape model (aspect ratio = 1).

	Acogel			Air-dried alcogel			Aerogel			Calcined aerogel		
	Mg	Ca	Sr	Mg	Ca	Sr	Mg	Ca	Sr	Mg	Ca	Sr
MaxEnt background (cm^{-1})	0.444	0.775	0.760	0.130	0.059	0.022	0.026	0.038	0.067	0.004	0.005	0.014
Start fit q (10^{-4} $Å^{-1}$)	8.883	8.883	8.883	37.96	37.96	35.34	8.883	8.883	11.42	43.63	43.63	64.58
End fit q ($Å^{-1}$)	0.050	0.059	0.040	0.202	0.230	0.223	0.262	0.311	0.200	0.449	0.267	0.289
Error multiplier	1.00	1.30	1.10	2.44	2.75	1.73	1.09	1.27	1.30	1.33	1.63	2.50
Mean size (nm)	18.3	26.2	20.3	9.0	26.7	27.9	35.3	5.7	25.0	4.6	25.6	34.8
Primary mode size (nm)	9.4	10.0	11.4	3.3	3.8	27.5	5.6	3.4	7.6	3.6	12.8	73.7
% of total volume fraction	44.6	27.6	49.6	21.7	4.6	82.7	8.2	69.8	11.9	76.2	7.4	84.6

effects may influence the accuracy of *MaxEnt* results is difficult to assess, but overall *MaxEnt* fit the data quite well even when peak-like features were present. The residuals were generally of smaller magnitude and more random compared with fits to the unified equation described previously.

Table 4 summarizes the results from the *MaxEnt* fits. The corresponding volume size distributions calculated by *MaxEnt* are compared for the Mg, Ca and Sr cation series in Figs. 6, 7 and 8, respectively. The three alcogels each exhibit a single narrow mode around 10 nm, but with a slight trend toward increasing modal size with increasing cation size. For Mg and Sr, both ambient and supercritical drying lead to a broadening of the distribution with the appearance of multiple modes. In the Ca series, this is only observed for the air-dried gel; the Ca aerogel exhibits a finer modal size relative to the alcogel. All air-dried gels exhibit a peak between 3 nm and 4 nm, which represents a reduction in size relative to the primary mode for the alcogel; however, we cannot rule out the possibility that these peaks could be artifacts, given their regularity and the fact that the indicated size represents the extreme limit of the SANS experimental range. *MaxEnt* indicates that Ca and Sr aerogels exhibit significant coarsening as a result of the heat treatment at 773 K. It should be noted, however, that *MaxEnt* shows the Sr sample simultaneously developing both a fine structure and a coarse structure, each of which persists and broadens after calcination.

4. Discussion

SANS data indicate a commonality of structure associated with the initial gel product for the Group II metal alkoxide hydrolysis reaction (Fig. 1). A power-law exponent of 1 is characteristic of scattering from one-dimensional (rod-like) objects (Porod, 1982). Under the present non-equilibrium hydrolysis conditions, the observation of exponents near unity could represent growth of quasi-linear fractal assemblies of

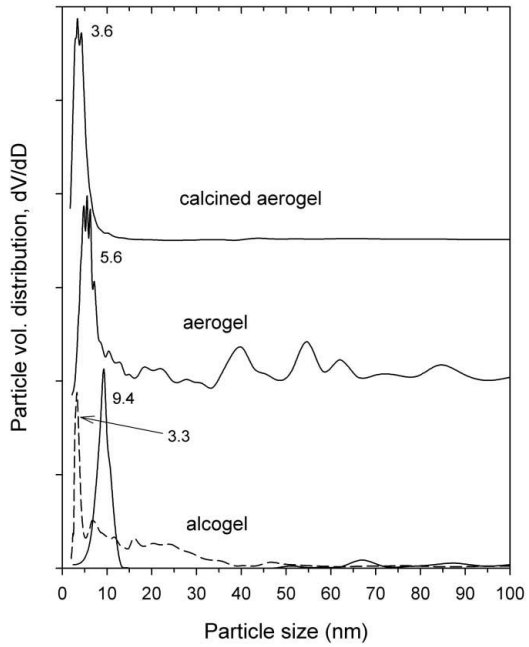

Figure 6
Calculated volume size distributions derived from a maximum entropy analysis of SANS data for the Mg hydroxide/oxide series. The dashed line corresponds to the air-dried alcogel. Numbers represent modal sizes in nm. Distributions for the aerogel and calcined aerogel have been scaled and offset to facilitate comparison.

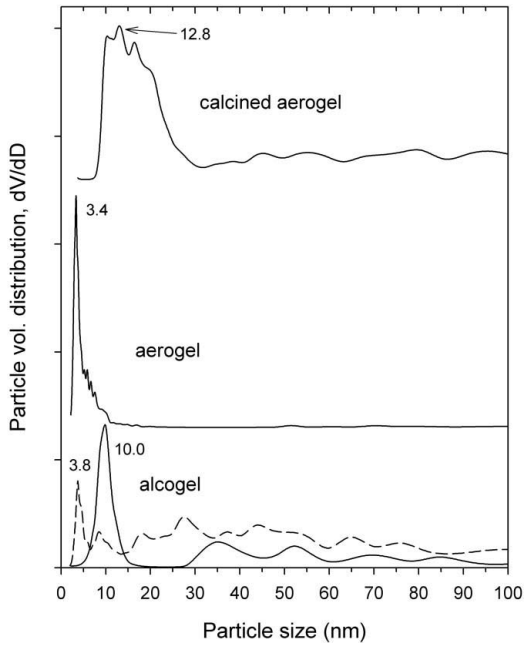

Figure 7
Calculated volume size distributions derived from a maximum entropy analysis of SANS data for the Ca hydroxide/oxide series. The dashed line corresponds to the air-dried alcogel. Numbers represent modal sizes in nm. Distributions for the aerogel and calcined aerogel have been scaled and offset to facilitate comparison.

primary crystallites, with linearity persisting over a limited length scale from about 1 to 20 nm. Low dimensionality may be a direct consequence of the crystalline nature of Group II cation hydrolysis products with a preferred orientation for coalescence, as suggested by TEM results for MgO (Richards *et al.*, 2000). Such ordered self-assembly is reminiscent of the oriented aggregation mechanism for crystal growth proposed by Banfield and coworkers for TiO_2 (see *e.g.* Penn & Banfield, 1998), and contrasts sharply with the more randomized growth mechanisms typically associated with noncrystalline hydrolysis products such as polymeric and colloidal silica (Schaefer, 1989). Oriented aggregation may in fact be a universal property for nanocrystal growth.

Diao *et al.* (2002) measured SAXS curves for a series of $Mg(OH)_2$ alcogels while varying the toluene/methanol (t/m) ratio. Their data were restricted to q values >0.02 Å^{-1} because of the limited experimental range of the 5 m pinhole camera used in their study. The authors extracted a power-law exponent for a region they identify as linear in log–log plots of their data. All toluene-containing samples yielded a power-law exponent of 1.8, while the sample without toluene produced an exponent of 2.2. The authors concluded that the hydrolysis product is a mass fractal down to molecular length scales characterized by a mass fractal dimension, $D_f = \alpha$. They speculate that toluene speeds up the hydrolysis reaction, shifting the kinetics from reaction-limited (t/m = 0, $D_f = 2.2$) to diffusion-limited (t/m > 0, $D_f = 1.8$) regimes. However, because of the truncation of their data at low q, a comparison with SANS results is difficult. It is also apparent that a significant incoherent SAXS background was not subtracted prior to the analysis, and this will greatly impact the high-q slope. The current SANS results do not support the high fractal dimensions found in this previous study.

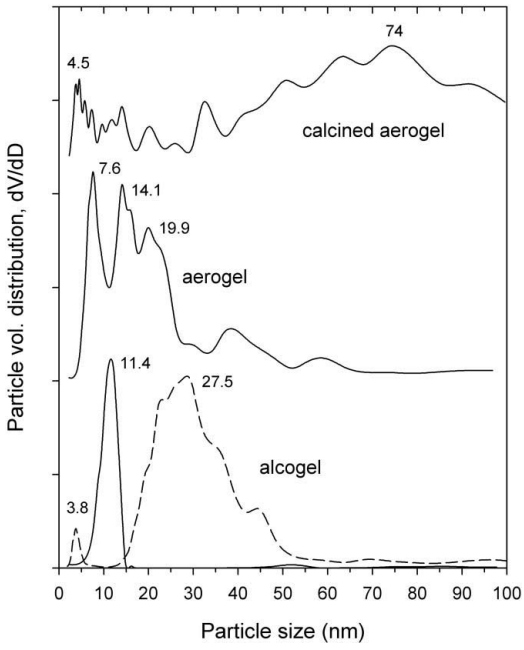

Figure 8
Calculated volume size distributions derived from the maximum entropy analysis of SANS data for the Sr hydroxide/oxide series. The dashed line corresponds to the air-dried alcogel. Numbers represent modal sizes in nm. Distributions for the aerogel and calcined aerogel have been scaled and offset to facilitate comparison.

Evaporative removal of the solvent at room temperature results in the disappearance of rod-like structure and the development of apparent fractally rough surface morphology represented by the extensive power-law regions in Fig. 2. Surface fractal scaling extends over nearly the same length scale range associated with the low-dimensional morphology in the wet gel. There is no evidence here to indicate that mass fractal structures exist, and the lack of rod-like scattering would initially seem to preclude the filiform (mesh-like) morphology that Diao *et al.* (2002) described for MgO alcogel air-dried on a TEM grid. We expect that the capillary forces that predominate during the final stages of subcritical drying should completely collapse the wet gel network and its linear components. This process produces a structure that behaves topologically like a highly folded surface characterized by D_S values in the 2.5 to 3 range. Subcritical drying of gels containing independent uniform particles more typically results in the formation of xerogels characterized by a close-packed quasi-ordered structure and producing strong correlation effects in the scattering data (Hackley *et al.*, 1992). For the smaller cations, Mg and Ca, the development of dominant surface fractal behavior, and lack of clear indications of ordering at length scales relevant to the primary crystallite size, would seem to suggest that the initial gel structure more closely resembles a polymer-like network of interconnected nanocrystal arrays and embedded polyhedra. Only the Sr gel, which produces a prominent correlation peak at low q in Fig. 2, gives a clear indication that some degree of particle-like ordering might exist, albeit on a relatively large length scale ($d \simeq 45$ nm). Maximum entropy results for the air-dried gel, and previously published TEM and XRD results for the calcined AP SrO (Medine *et al.*, 2002), lend support to the idea of a close-packed large particle structure for the Sr system, indicating particle sizes in the roughly 20 to 100 nm range (much coarser than either Mg or Ca). The large globules giving rise to the observed correlation effects could consist of multiple nanocrystalline domains, but they clearly exhibit surface fractal roughness on smaller length scales, a property common to the hydroxides of all three Group II cations studied in this investigation.

Scattering by supercritically dried aerogels is similarly dominated by surface fractal-like behavior (Fig. 3), but here the individual scattering curves exhibit significant variation in form. It appears that the aerogel drying process has a topologically dissimilar impact on structure development for the three cations. The absence of a systematic variation in the SANS data suggests that a simple linear effect related to cation size cannot account for the observed differences. The AP hydroxide powders are subjected to higher temperatures during the supercritical drying process (up to 538 K) compared with air-dried samples, and this probably has some additional impact on the solid phase. Certainly, these temperatures are sufficient to promote partial dehydration,

and this may in turn facilitate larger-scale structural changes during supercritical drying.

Of particular note regarding this system is the observation that both subcritical and supercritical drying produce materials that lack any sign of underlying nanoscale mass fractal structure. This lies in clear contrast with sol–gel-produced amorphous silica, where the kinetic growth mechanisms tend to yield mass fractal aggregates or polymer networks whose ramified structures are preserved largely intact following supercritical drying (Schaefer, 1989), but are lost when solvent is evaporated subcritically. We attribute this difference in structural development to the ionic nature of Group II hydroxides and oxides, which promote formation of a crystalline geometry with preferred orientations for growth and coalescence. Crystal coalescence may also contribute directly to preserving the high surface areas typically associated with sol–gel materials. In the case of $Mg(OH)_2$, subcritical drying produces a specific surface area comparable to supercritically dried material (Diao *et al.*, 2002). We speculate that coalescence of nanocrystals in preferred orientations may help prevent the capillary-driven collapse and subsequent loss of surface area by increasing the rigidity and strength of local interparticle connections.

To obtain the metal oxide phase, the aerogel powders produced during supercritical drying are calcined at 773 K under dynamic vacuum. This treatment results in complete dehydration with transformation to periclase, removal of most residual methoxide groups and an increase in crystallinity (Utamapanya *et al.*, 1991). Although surface-area measurements for AP $Mg(OH)_2$ and AP MgO (see Table 1) suggest that calcining can also induce some coarsening, this effect varies with the metal cation and is highly temperature dependent. For example, the surface area reported for AP CaO typically increases during calcining as a result of the blossoming phenomenon mentioned previously (Koper *et al.*, 1997).

A comparison of the scattering curves for the calcined oxides (Fig. 4) with those obtained for the corresponding aerogels (Fig. 3) indicates that high-temperature treatment has a sizable impact on the development of nanoscale structure in these materials. MgO and CaO develop correlation peaks that correspond to liquid-like ordering on length scales of $d \simeq 6$ nm and $d \simeq 20$ nm, respectively. For AP MgO this value is consistent with XRD and TEM estimates for primary particle size, suggesting that local packing of primary crystallites is somehow facilitated by the dehydration process. For AP CaO, the value of d is quite a bit larger than the reported crystallite size range, but the wide variation in reported surface areas for AP CaO suggests that the few reported size measurements on which this range is based may not be representative of the true range. Richards *et al.* (2000) report a similar maximum in their SAXS data for AP MgO; however, they interpret this feature as a Guinier region, and assume a Porod slope for the high-q limit. From a fit of their data to the unified equation they obtain $R_g = 3.9$ nm for the primary particles. But more importantly, they report that this maximum is absent in SAXS curves measured after compacting the powders into pellets under high pressure. They attribute the disappearance of the peak-like feature to disruption of the micrometer-size aggregates visible under low-magnification TEM prior to compaction. This rationale cannot be strictly applied, since exponential Guinier scattering from particles (aggregates) of micrometer size would be observed at much lower q values relative to the high-q value associated with the observed maximum ($\sim$0.1 Å^{-1}). On the other hand, if we assume that this maximum represents a correlation effect, as indicated by SANS data, its disappearance following compaction indicates that nanoscale structural changes must accompany the forced rearrangement and interpenetration processes that occur under high pressure. Interestingly, when we fit our SANS data using the unified Guinier/power-law equation, resulting R_g values for the primary particles yield equivalent spherical diameters (6 and 19 nm for AP MgO and CaO, respectively) that are almost identical to the d values calculated from the peak positions using the Bragg formula.

MgO is the only AP sample we examined that gave any indication of having a final slope close to -4, which would indicate a sharp interface at molecular dimensions. Unfortunately, the relevant high-q region is shortened by a combination of instrumental resolution limitations and incoherent background scattering, making it impossible to determine the slope accurately. Allowing the final slope to vary while fitting the data using the unified equation results in a power-law exponent of 5, which seems physically unreasonable for this system; exponents >4 are indicative of a diffuse interface, which might apply for instance to a surface with an adsorbed surfactant. On the other hand, it is reasonable to assume that calcining leads to some smoothing of the aggregate surface, such that the surface fractal scattering displayed by the aerogel is attenuated upon high-temperature treatment. As previously mentioned, Vacher *et al.* (1988) observed this smoothing effect upon heat-treatment of silica aerogels. Although this explanation would appear at first glance less probable in the case of crystalline MgO, with its high melting point (3103 K), Mel'gunov *et al.* (2003) have recently observed the onset of sintering (*i.e.* surface area decrease, particle size increase, particle number decrease) in AP MgO under dynamic vacuum at temperatures above about 673 K. Sintering in this system may be enhanced by the relatively high density of defect and edge sites present, which accelerate mass transport at crystal surfaces and grain boundaries, and by the small diffusion distances involved. For instance, it has been shown that peroxy defects associated with Mg^{2+} vacancies in MgO thermally dissociate at temperatures above 673 K to produce unbound oxygen holes that diffuse to the surface (Freund *et al.*, 1989). The presence of such vacancies and other highly mobile point defects and edge sites may be directed to promote energetically more favorable morphologies through solid-state diffusion at temperatures substantially lower than, and at rates significantly higher than, those of materials lacking these defects. Sintering would likely result in a reduced surface roughness. It still remains to be explained why SrO and possibly CaO, with lower melting points than MgO, show

persistent surface-fractal-like scattering at small length scales following an identical treatment at 773 K.

A maximum entropy analysis of SANS data produced fits of consistent quality, but yielded a complex picture of structure development if viewed in isolation. The results imply that different structural pathways exist for the three cations. Although the *MaxEnt* fits for all three alcogels yield a single narrow mode around 10 nm, the similarities end at that point. The subsequent fits for the dried and calcined materials produce drastically different volume distributions for each metal cation. So, although the initial hydrolysis products share similar physical dimensions, maximum entropy indicates that they respond very differently to the drying and calcining processes to which they are subsequently subjected. A clear systematic dependence cannot be correlated to cation size, although the sharpness and uniformity of the calculated distributions generally decrease in going from Mg to Ca to Sr. Clearly, AP MgO retains more of its initial nanoscale characteristics than the other two oxides, a fact that is consistent with previously reported physical data for this system. Maximum entropy results indicate a slight decrease in the modal size and a refinement in the distribution for AP MgO following calcining. The broad tail in the distribution evident in the aerogel has all but disappeared in the oxide, leaving a single primary mode, representing about 83% of the total volume distribution. In contrast, AP SrO undergoes a bifurcation during the drying and calcining processes, simultaneously developing both finer and coarser modes relative to the initial hydrolysis product. This bifurcation is consistent with TEM results that indicate that AP SrO has a complex hierarchical structure characterized by multiple length scales and crystal habits. Size distributions for the Ca series lie between these two extremes, developing similarly to Mg in the alcogel-to-aerogel transition, but coarsening considerably during the calcining treatment.

5. Concluding remarks

Results indicate that the hydrolysis product formed by the addition of excess water to a methanolic solution of Group II metal methoxide in the presence of toluene is characterized by rod-like morphology at length scales below 20 to 30 nm. Large scattering domains of indeterminate structure are evident from the low-q data. Evidence for mass fractal scaling was not found for any of the processed powders examined in this study. On the contrary, surface fractal scattering was found to be the most dominant feature. We found that the surface fractal dimension, D_S, calculated from the measured power-law exponent, tended to decrease with treatment temperature, indicating that a progressively sharper interface results from progressive dehydration and sintering. For example, a D_S of 3 (maximally rough surface) was determined for the $Mg(OH)_2$ alcogel dried under ambient conditions, while the aerogel-processed sample (dried at 538 K under high pressure) gave a value of 2.4, and the calcined oxide (treated at 773 K under dynamic vacuum) has an apparently smooth surface with D_S = 2 (Porod scattering). We would expect the existence of fractal surface structures to have consequences relative to surface availability and perhaps overall reactivity of the aerogel material.

A recent suggestion by Diao *et al.* (2002) that supercritical drying of Group II hydroxides may be an unnecessary step to obtain high-surface-area precursor powders, though technically correct, does not consider the impact that drying might have on the subsequent high-temperature treatment necessary in order to obtain the reactive, technologically important oxide phase. SANS results show that qualitative differences in structure exist between air-dried and supercritically dried gels, irrespective of their measured surface areas. Furthermore, evidence for local close-packing of crystallites in the air-dried gels suggests that crystal growth might be promoted in these materials if subjected to high temperature, due to a more compact crystallite arrangement compared with the aerogel-processed powders. The possible impact of subcritical drying on structure development during calcining has not been examined to our knowledge, but may be worth pursuing.

We attribute the apparent absence of mass fractal structure in this system, and the similarity in surface areas reported for subcritically and supercritically dried $Mg(OH)_2$ powders, to the underlying nanocrystalline nature of the Group II hydroxides and oxides. Evidence exists for oriented coalescence of nanocrystals as the basis for development of polyhedral and low-dimensional arrays. This contrasts with the widely reported mass fractal properties associated with amorphous aerogel-processed silica.

The authors wish to thank the NIST Center for Neutron Research for access to the NG-7 neutron beamline. We are grateful to the National Science Foundation and the Army Research Office (DARPA MURI contract DAAD 19-01-1-0619) for financial support. We thank A. Allen (NIST) and J. Ilavsky (Argonne National Laboratory) for useful discussions on implementing the scattering evaluation and modelling software used in this study. One author (VAH) also acknowledges support for this work by a NIST Materials Science and Engineering Laboratory Director's Reserve award.

References

Bale, H. D. & Schmidt, P. W. (1984). *Phys. Rev. Lett.* **53**, 596–599.
Beaucage, G. (1995). *J. Appl. Cryst.* **28**, 717–728.
Beaucage, G. (1996). *J. Appl. Cryst.* **29**, 134–146.
Chadwick, A. V., Poplett, I. J. F., Maitland, D. T. S. & Smith, M. E. (1998). *Chem. Mater.* **10**, 864–870.
Choi, S.-M., Barker, J. G., Glinka, C. J., Cheng, Y. T. & Gammeld, P. L. (2000). *J. Appl. Cryst.* **33**, 793–796.
Diao, Y., Walawender, W. P., Sorensen, C. M., Klabunde, K. J. & Rieker, T. (2002). *Chem. Mater.* **14**, 362–368.
Freund, M. M., Friedemann, F. & Batllo, F. (1989). *Phys. Rev. Lett.* **19**, 2096–2099.
Glinka, C. J., Barker, J. G., Hammouda, B., Krueger, S., Moyer, J. J. & Orts, W. J. (1998). *J. Appl. Cryst.* **31**, 430–445.

Guinier, A. & Fournet, G. (1955). *Small Angle Scattering of X-rays.* New York: John Wiley.
Hackley, V. A., Anderson, M. A. & Spooner, S. (1992). *J. Mater. Res.* **7**, 2555–2571.
Ilavsky, J. (2004). *Irena 1 SAS Modeling Macros Manual.* Advanced Photon Source, Argonne National Laboratory.
Itoh, H., Utampanya, S., Stark, J. V., Klabunde, K. J. & Schulp, J. R. (1993). *Chem. Mater.* **5**, 71–77.
Jemian, P. R. (1995). *User Guide for Sizes: a Small-Angle Scattering Analysis Program.* Advanced Photon Source, Argonne National Laboratory.
Keefer, K. D. & Schaefer, D. W. (1986). *Phys. Rev. Lett.* **56**, 2376–2379.
Khaleel, A., Kapoor, P. N. & Klabunde, K. J. (1999). *Nanostruct. Mater.* **11**, 459–468.
Klabunde, K. J. & Mulukutla, R. S. (2001). *Nanoscale Materials in Chemistry*, edited by K. J. Klabunde, pp. 223–261. New York: Wiley Interscience.
Klabunde, K. J., Stark, J., Koper, O., Mohs, C., Park, D. G., Decker, S., Jiang, Y., Lagadic, I. & Zhang, D. (1996). *J. Phys. Chem.* **100**, 12142–12153.
Koper, O. & Klabunde, K. J. (1993). *Chem. Mater.* **5**, 500–505.
Koper, O. B., Lagadic, I., Volodin, A. & Klabunde, K. J. (1997). *Chem. Mater.* **9**, 2468–2480.
Li, Y. X., Koper, O., Atteya, M. & Klabunde, K. J. (1992). *Chem. Mater.* **4**, 323–330.
Long, G. G., Krueger, S., Jemian, P. R., Black, D. R., Burdette, H. E., Cline, J. P. & Gerhardt, R. A. (1990). *J. Appl. Cryst.* **23**, 535–544.
Lucas, E. M. & Klabunde, K. J. (1999). *Nanostruct. Mater.* **12**, 179–182.
Martin, J. E. (1986). *J. Appl. Cryst.* **19**, 25–27.
Medine, G. M., Klabunde, K. J. & Zaikovski, V. (2002). *J. Nanopart. Res.* **4**, 357–366.
Medine, G. M., Zaikovski, V & Klabunde, K. J. (2004). *J. Mater. Chem.* **14**, 757–763.
Mel'gunov, M. S., Fenelonov, V. B., Mel'gunova, E. A., Bedilo, A. F. & Klabunde, K. J. (2003). *J. Phys. Chem. B*, **107**, 2427–2434.
National Institute of Standards and Technology Center for Neutron Research (2002). *NG3 and NG7 30-meter SANS Instruments Data Acquisition Manual.*
Nieves, I. & Klabunde, K. J. (1988). *Mater. Chem. Phys.* **18**, 485–498.
Penn, R. L. & Banfield, J. F. (1998). *Science*, **281**, 969–971.
Pfeifer, P & Avnir, D. (1983). *J. Chem. Phys.* **79**, 3558–3565.
Porod, G. (1982). In *Small Angle X-ray Scattering*, edited by O. Glatter & O. Kratky, pp. 17–51. New York: Academic Press.
Potton, J. A., Daniell, G. J. & Rainford, B. D. (1988). *J. Appl. Cryst.* **21**, 663–668.
Richards, R., Li, W., Decker, S., Davidson, C., Koper, O., Zaikovski, V., Volodin, A., Rieker, T. & Klabunde, K. J. (2000). *J. Am. Chem. Soc.* **122**, 4921–4025.
Rywak, A. A., Burlitch, J. M. & Loehr, T. M. (1995). *Chem. Mater.* **7**, 2028–2038.
Schaefer, D. W. (1989). *Science*, **243**, 1023–1027.
Schmidt, P. W. (1988). *Makromol. Chem. Macromol. Symp.* **15**, 153–166.
Stark, J. V., Park, D. G., Lagadic, I. & Klabunde, K. J. (1996). *Chem. Mater.* **8**, 1904–1912.
Stoimenov, P. K., Klinger, R. L., Marchin, G. L. & Klabunde, K. J. (2002). *Langmuir*, **18**, 6679–6686.
Stoimenov, P. K., Zaikovski, V. & Klabunde, K. J. (2003). *J. Am. Chem. Soc.* **125**, 12907–12913.
Tatchev, D. & Kranold, R. (2004). *J. Appl. Cryst.* **37**, 32–39.
Utamapanya, S., Klabunde, K. J. & Schlup, J. R. (1991). *Chem. Mater.* **3**, 175–181.
Vacher, R., Woignier, T. & Pelous, J. (1988). *Phys. Rev. B*, **37**, 6500–6503.
Wagner, G. W., Bartram, P. W., Koper, O. & Klabunde, K. J. (1999). *J. Phys. Chem. B*, **103**, 3225–3228.
Wyckoff, R.W.G. (1963). In *Crystal Structures*, Vol. 1. New York: John Wiley.
Zhang, H., Penn, R. L., Hamers, R. J. & Banfield, J. F. (1999). *J. Phys. Chem. B*, **103**, 4656–4662.
Znaidi, L., Chhor, K. & Pommier, C. (1996). *Mater. Res. Bull.* **31**, 1527–1535.